6

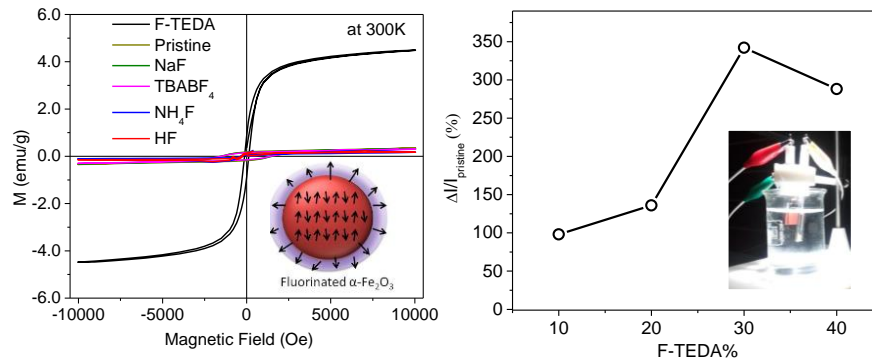# Fluorinated α-Fe$_2$O$_3$ Nanostructures and Applications

6.1 Introduction

6.1.1 Fluorination of Metal Oxide Nanostructures

Metal oxides nanostructures have been used as an active material in various applications such as batteries, solar cells, supercapacitors, sensors, coatings, paints, water treatment, etc. [Chavali et al., 2019]. Metal oxides nanomaterial can be tuned by various methods for interesting electrical, optical, mechanical, and chemical properties. However, scientists all around the globe are working on tuning the properties of metal oxides as there is still much more space that needs to be discovered [Medhi et al., 2020]. Fluorination of metal oxides nanoparticles has gained importance due to the incorporation of unique and exciting properties. Fluorinated nanomaterials can demonstrate unique and unexpected electrical, mechanical, optical, magnetic, catalytic, and electrochemical properties. The anion substitution, which influences the electronic state of the metal and crystal field, can tune the structures as well as physiochemical properties. The changes in ionic bonding and valence state can induce different properties from that of metal oxides or pure fluorides and thus opening up the doors in various applications [Deng, 2017].
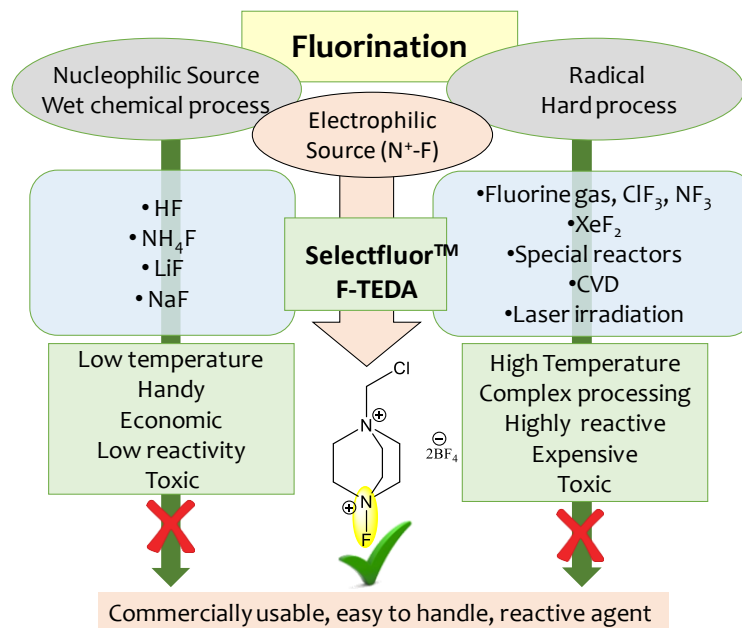

Figure 6.1 Various precursors and methods used for fluorination of metal oxides.

6.1.1 Objectives of Work

As described in detail in section 6.1.1 and 6.1.2, fluorination of metal oxide nanoparticles has usually been performed using nucleophilic or radical sources. Nucleophilic sources are easy to handle and solution-processable precursors; however, using these usually lead to oriented growth rather than fluorination of nanomaterial taking place. On the other hand, fluorination of nanomaterials using a radical precursor require very high temperature, costly equipment and are very dangerous to handle. In an effort to solve this issue, fluorination of α-Fe$_2$O$_3$ is performed using N$^+$-F containing an organo-fluorine compound F-TEDA, Selectfluor™ (Figure 6.1). The objectives of the work are as follows:

1. To perform in-situ fluorination of α-Fe$_2$O$_3$ using F-TEDA and other conventional fluorinating agents as control.
2. To perform detailed chemical, structural, and morphological analysis of the fluorinated α-Fe$_2$O$_3$ nanostructures.
3. To study the effect of fluorination on magnetic properties of fluorinated α-Fe$_2$O$_3$.
4. To test fluorinated α-Fe$_2$O$_3$ as a photoanode in photoelectrochemical cells.

6.2 Experimental

6.2.1 Materials

Fluorinated α-Fe$_2$O$_3$ was synthesized by hydrothermal process using K$_3$[Fe(CN)$_6$] precursor (15 mM) in a closed Teflon vessel of 100 mL capacity at 140 °C for 48 hrs. A co-addition of 10, 20, 30, and 40 weight% of F-TEDA and HF while 20 weight% of sodium fluoride (NaF), ammonium fluoride (NH$_4$F) and tetrabutylammonium tetrafluoroborate (TBABF$_4$) was performed with respect to K$_3$[Fe(CN)$_6$] precursor. After the reaction, the products formed were separated by centrifugation and repeatedly washed with water and ethanol for washing the by-products. The weight percentages are chosen initially for F-TEDA such that the changes in properties are visibly observable, and a moderate weight percentage of fluorinating agents is chosen for comparison with F-TEDA. The fluorination reaction is performed using different fluorinating agents (Figure 6.2) in-situ with the Fe precursor during hydrothermal growth conditions. F-TEDA is a source of electrophilic fluorine (F$^+$), whereas HF is for fluoride (F$^-$) species. F-TEDA possesses two sources of fluorine, the fluoronium ion bonded to N in the cationic form and tetrafluoroborate (BF$_4^-$). To bring out the F$^+$ contribution in F-TEDA, TBABF$_4$ with counter BF$_4^-$ anion is used for comparison. The nature of F$^+$ is also contrasted with F$^-$ by using H$^+$F$^-$, NH$_4^+$F$^-$, Na$^+$F$^-$ as different fluorinating agents.
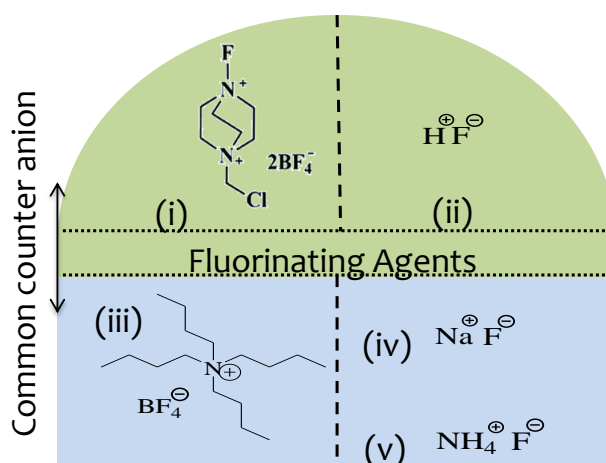

Figure 6.2: Schematic showing (i) F-TEDA and (ii) HF used as fluorinating agents in the study. Other fluorinating species with common fluorine containing counter anions (iii) TBABF$_4$ and (iv) NaF (v) NH$_4$F are used as control in comparison to F-TEDA and HF, respectively.

6.2.2. Characterization

The samples synthesized in this study are characterized by XRD technique for structural and phase identification. The sample preparation for XRD was carried out by grinding the samples in mortar-pestle to avoid any preferred orientation. The samples are taken in the powder form, and the XRD pattern is recorded in the 2θ range of $20°$ to $80°$ at a scan rate of $0.05°/s$. The crystallite size is calculated using the Scherrer formula [Patterson, 1939], $\tau = k\lambda/\beta cos\theta$ where τ is mean size of ordered crystalline, k is shape factor typical value 0.9, λ is the wavelength of X-ray, β is line broadening (FWHM) and θ is Bragg angle. The 110 and 104 peaks are fitted using origin software for analysis. Scanning Electron Microscope (SEM) imaging was performed using Zeiss EVO 18 Special Edition microscope equipped with an EDAX detector. The specific surface area was analyzed by N_2 adsorption-desorption isotherm (Quntachrome autosorb iQ$_3$).

6.2.3. Magnetic Measurements

Magnetic Measurements were performed using SQUID magnetometer (Ever Cool MPMS XL, Quantum Design, 2002). M-H curves are measured in the field range ±10,000 Oe at a temperature of 20 K and 300 K while M-T measurements are done from 20 K to 300 K at an applied field of 500 Oe and under zero-field. The SQUID magnetometer results were obtained with an accuracy of 10^{-6} emu despite of intrinsic sensitivity of $\sim 5 \times 10^{-9}$ emu. The difference could be due to the intrinsic artifacts which stem from the inherent design of the magnetometer as well as potential issues related with the measurement. The M-H measurements are subtracted with the diamagnetic contribution of the sample holder.

6.2.4. Photoelectrochemical Measurements

The films of α-Fe$_2$O$_3$ and fluorinated α-Fe$_2$O$_3$ were prepared by three-layer screen printing on FTO glass for photoelectrochemical measurements. The paste of appropriate viscosity was prepared by mixing 0.05 g of ethylcellulose, 0.3 mL of α-terpinol, and 0.02 mL glacial acetic acid in a mortar and pestle for 30 min. Upon complete dissolution of ethylcellulose, 0.1 g of hematite was added and mixed for 10 min. Further, an appropriate amount of ethanol was added for viscosity adjustment. The prepared paste was layer by layer coated on FTO glass using 100 mesh screen and squeegee. Every layer was dried before coating successive layer. The prepared films were further annealed at 500 °C for 5 h before using for electrochemical measurements. Electrochemical workstation (CHI6600) was used for I-V measurements in a three-electrode setup using Pt mesh as counter electrode and Ag/AgCl (3 M KCl) as a reference electrode. The potentials were converted to the reversible hydrogen electrode (RHE) scale using the standard Nernst equation. Chronoamperometry experiments were performed at 0.6 V versus Ag/AgCl (1.6 V versus RHE). The measurements were performed under illumination of 100 W/m^2 (one-tenth of 1 Sun) while the light source was switched on and off after every 5 s. The photocurrent value at the end of the chronoamperometry measurement was taken as the steady-state photocurrent and was used to compare different samples.

6.3 Result and Discussion

6.3.1 Oriented Growth of α-Fe$_2$O$_3$

The influence of fluorination on the structural properties is examined by XRD patterns (Figure 6.3). As seen in the figure, the XRD patterns corresponding to different fluorinated samples (20% by weight relative to Fe precursor) resembles pristine α-Fe$_2$O$_3$ and rhombohedra structure of hematite (JCPDS data card number 86-0550) [Das et al., 2015] without origin of any new peaks except minor impurity peak in case of HF.
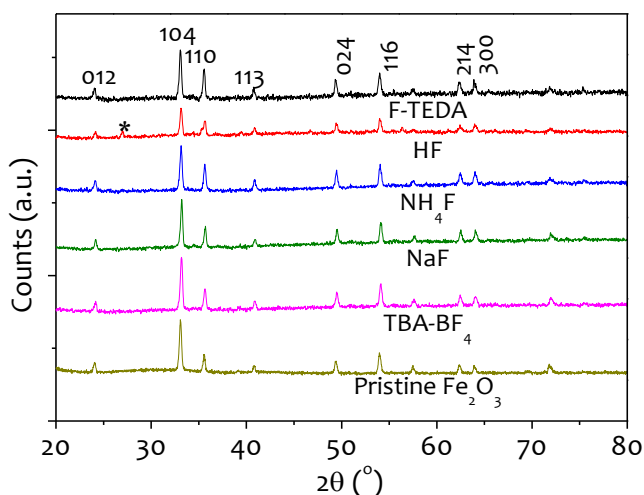
Figure 6.3 XRD patterns of α-Fe_2O_3 synthesized with 20% by weight of different fluorinating agents.

This implies that the different fluorinating agents (F-TEDA, HF, NH_4F, NaF, and $TBABF_4$) do not alter the crystalline structure and phase of α-Fe_2O_3 and probably acts as the growth directing agents. No systematic variation could be observed in the crystallite size upon fluorination with F-TEDA, NH_4F, NaF, and $TBABF_4$. The average crystallite size calculated using the Scherer formula for pristine and fluorinated α-Fe_2O_3 along (104) and (110) is ~28.6± 4.9 nm and 28.8± 6.8 nm, respectively.
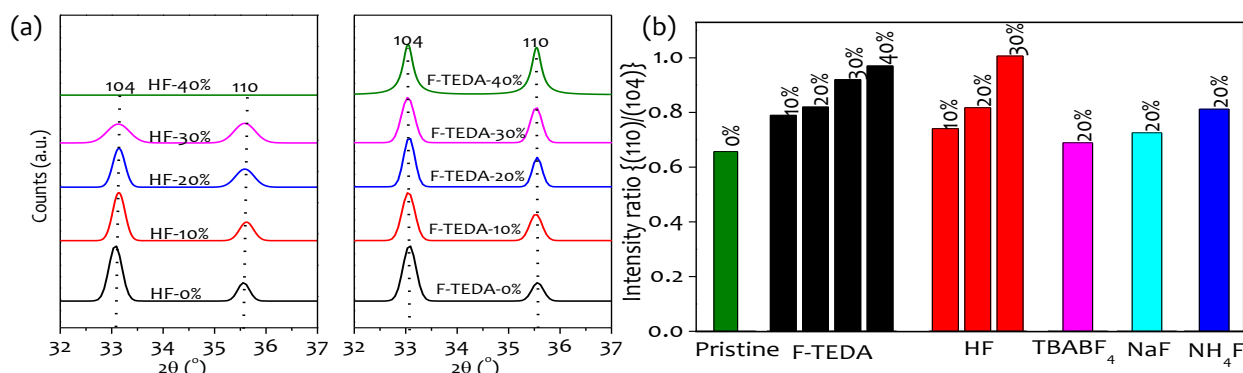

Figure 6.4: (a) XRD patterns of α-Fe_2O_3 fluorinated with 0%, 10%, 20%, 30% and 40% by weight of HF and F-TEDA. (b) Intensity ratio of (110)/(104) peak intensities of α-Fe_2O_3 for all fluorinating agents.

Interestingly, the orientation of α-Fe_2O_3 along (104) and (110) plane is influenced systematically upon fluorination with HF and F-TEDA (Figure 6.4a). As HF concentration is increased gradually, the (104) plane intensity decreases and the peak becomes broad due to smaller crystallite size. At 40% HF, the α-Fe_2O_3 nanostructures are completely etched out. Whereas in case of F-TEDA, the (110) peak intensity increases in α-Fe_2O_3 probably due to preferred orientation along this direction. Later is particularly interesting due to isotropic conduction along (110) growth direction similar to that observed for vertically aligned α-Fe_2O_3 nanowires in literature [Kim et al., 2006]. Peak analysis in Figure 6.4b shows that F-TEDA and HF result in an enhanced (110) with respect to (104) peak intensity however, enhancement is due to growth along (110) in case of F-TEDA while etching along (104) in case of HF. Among others, NH_4F has a relatively higher ratio as compared to NaF and $TBABF_4$. The increase in (110) peak intensity in case of F-TEDA is due to the growth along {11$\overline{2}$0} planes [Green et al., 2017].

The influence of different fluorides on the crystallization process and morphology of the α-Fe_2O_3 can be seen by the SEM images in Figure 6.5. The growth mechanism was greatly affected in case of F-TEDA and HF. SEM images in Figure 6.5a and b clearly reveal the differences in the morphology and size resulting from the fluorination performed under identical hydrothermal conditions. The relative size of dendrites increases in the presence of F-TEDA, indicating higher growth rates. The increase in dendritic size in case of F-TEDA can be attributed to F^+ ions, which

facilitate the growth mechanism. Whereas in HF and NH$_4$F, the dendrite-shaped α-Fe$_2$O$_3$ possesses sharp features with a reduction in size due to considerable etching (Figure 6.5c,d).
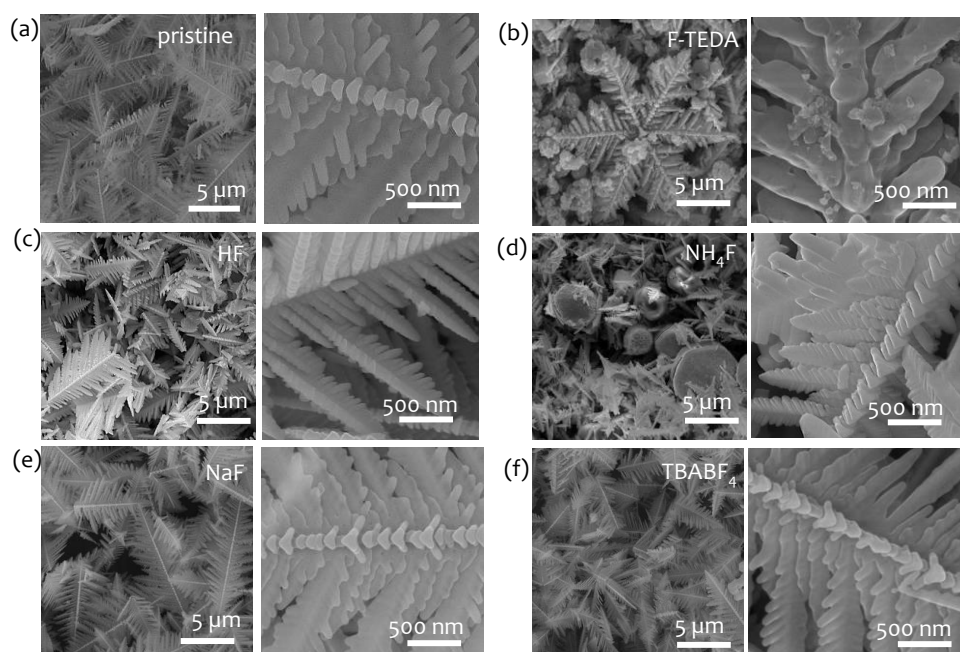

Figure 6.5: SEM images of (a) pristine α-Fe$_2$O$_3$, (b) F-TEDA-20%, (c) HF-20%, (d) NH$_4$F-20%, (e) NaF-20% and (f) TBABF$_4$-20% mediated α-Fe$_2$O$_3$ synthesis.

In literature, F$^-$ from HF and NH$_4$F is known for resulting in an increase in 110 peak, which is concomitant with Figure 6.5d as well [Yamamoto et al., 2010]. In case of NH$_4$F, there is even the presence of spherical and faceted structures along with dendrites, probably due to site-selective etching. However, TBABF$_4$ and NaF act as neutral without affecting the α-Fe$_2$O$_3$ dendrite growth (Figure 6.5e,f). Clearly, difference is due to the electrophilic fluorine in case of F-TEDA that leads to directional growth of α-Fe$_2$O$_3$ whereas fluoride species (nucleophilic) act as an etchant and seems to inhibit the self-aggregation and prevent its further growth. The sizes observed in the SEM is different from the crystallite size computed with Scherrer formula since the dendritic structures seen in the SEM images consist of a hierarchical assembly of α-Fe$_2$O$_3$ nanoparticles.

6.3.2 Estimation of Fluorine in α-Fe$_2$O$_3$

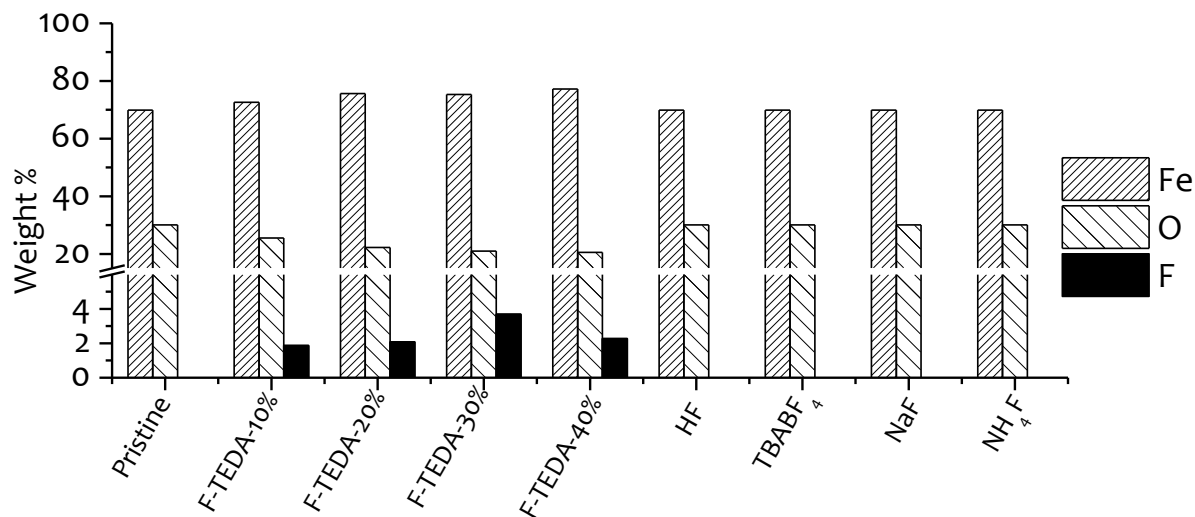**Figure 6.6:** Elemental composition of α-Fe$_2$O$_3$ fluorinated with different fluorinating agents.

The fluorine content is estimated by EDS analysis in all cases (Figure 6.6). Interestingly, F-TEDA-20% shows fluorine content of ~2.08 wt% in α-Fe$_2$O$_3$, whereas no fluorine is detected for

α-Fe$_2$O$_3$ synthesized with HF, NH$_4$F, NaF, and TBABF$_4$. Probably, fluorine content is too low to be detected by EDS studies in these cases. In case of F-TEDA, the morphological evolution along (110) growth direction takes place, resulting in six-fold symmetry. The maximum fluorine content of 3.69 wt% is obtained for 30% F-TEDA while it decreases to 2.27% in the case of 40% F-TEDA.
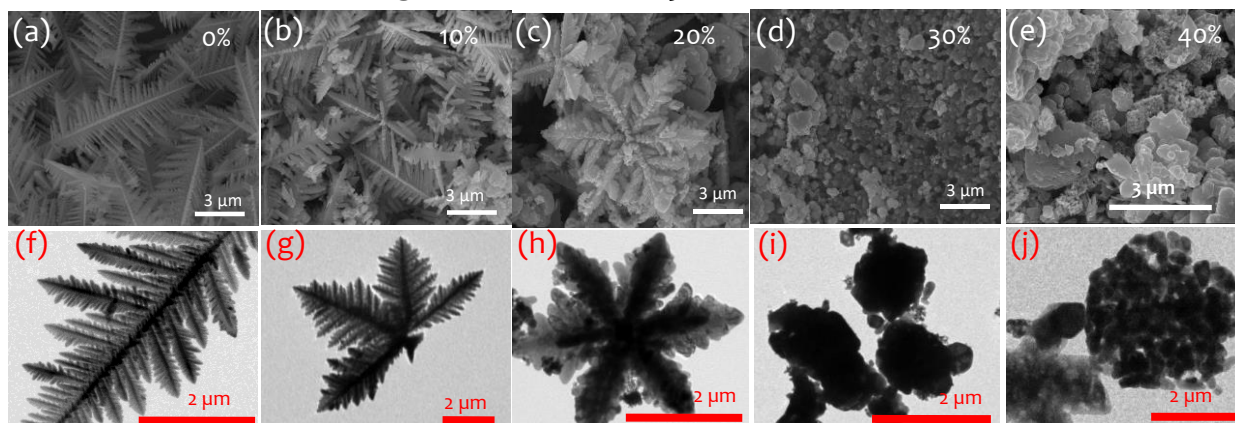
6.3.3 Structure and Morphology: Dendritic α-Fe$_2$O$_3$

Figure 6.7: (a-e) FESEM images and corresponding (f-j) Transmission Electron Microscopy images of pristine and α-Fe$_2$O$_3$ with 10%, 20%, 30% and 40% of F-TEDA respectively.

The pristine and α-Fe$_2$O$_3$ synthesized using different concentrations of F-TEDA in precursor solution is characterized by FESEM and TEM imaging (Figure 6.7). It can be observed that pristine α-Fe$_2$O$_3$ has a typical dendrite type structure (Figure 6.7a,f) with the backbone oriented in [1100] direction. The surface structure of α-Fe$_2$O$_3$ undergoes modification by the systematic introduction of F-TEDA in the reaction mixture. At 10% F-TEDA, some of the dendrite structures start assembling along four directions (Figure 6.7b, g). When 20% F-TEDA was added to the reaction mixture, α-Fe$_2$O$_3$ exhibited a clear change in shape from single dendrite to a snowflake-type nanostructure with six-fold symmetry (Figure 6.7c, h). At much higher F-TEDA concentration (30% or more), the growth rate is accelerated in all crystallographic directions resulting in loose aggregates of nanoparticles (Figure 6.7d, e, i, j).
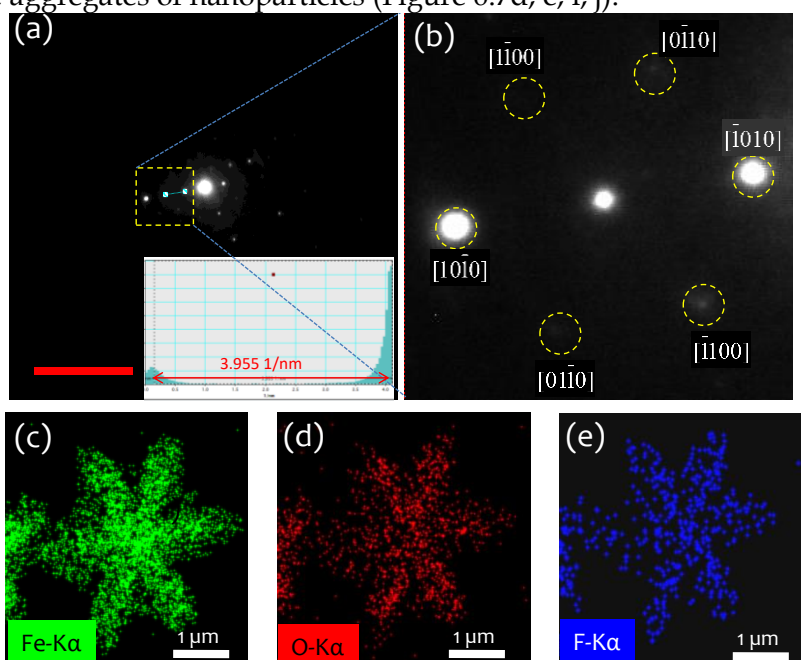

Figure 6.8: (a,b)Selected Area Electron Diffraction pattern at low and high magnification and (c-e) Energy Dispersive Spectroscopy (EDS) imaging of α-Fe$_2$O$_3$ with 20% F-TEDA.

The α-Fe$_2$O$_3$ synthesized with 20% of F-TEDA is further examined in detail. The electron diffraction pattern with zone axis [0001] shows the hexagonal reciprocal lattice of the corresponding snowflake-type structure. The inter-planar distance of 0.2528 nm corresponds to the {1120} family of planes growing in [1100] family direction (Figure 6.8a, b). The EDS maps of Fe-Kα, O-Kα, and F Kα corresponding to the TEM images in Figure 6.8c-e exhibit uniformly distributed signals indicating that fluorine is uniformly covering the surface of α-Fe$_2$O$_3$.

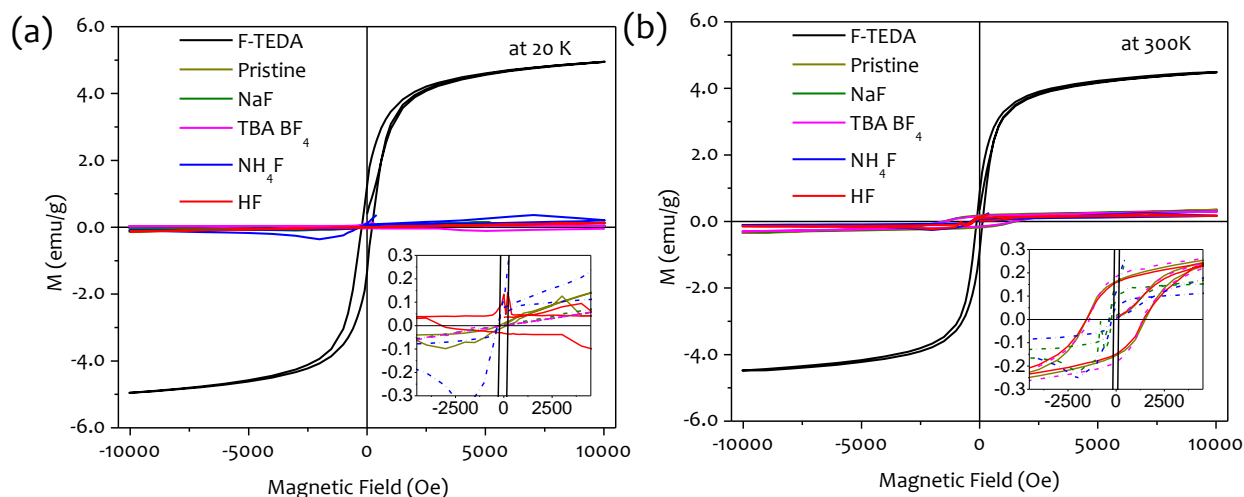## 6.3.4 Ferromagnetic Behaviour of Fluorinated α-Fe$_2$O$_3$

Figure 6.9: Magnetic hysteresis loops (M-H curves) of pristine α-Fe$_2$O$_3$ and α-Fe$_2$O$_3$ fluorinated with F-TEDA-20%, HF-20%, NH$_4$F-20%, TBABF$_4$-20% and NaF-20% at (a) 20 K and (b) 300 K respectively.

The magnetic properties of α-Fe$_2$O$_3$ before and after fluorination exhibit interesting features as studied by the M-H data at 20 K and 300 K (Figure 6.9a, b). As observed in Figure 6.9a, pristine α-Fe$_2$O$_3$ is antiferromagnetic at 20 K without any magnetic moment. However, due to local deviations from the compensation due to defects, frozen or pinned uncompensated moments give rise to the magnetic moment in antiferromagnets (Figure 6.9b). The weak magnetization observed in pristine Fe$_2$O$_3$ could be attributed both to the size induced uncompensated magnetization and the spin canting in an otherwise antiferromagnetic material. Interestingly, α-Fe$_2$O$_3$ fluorinated with F-TEDA exhibits a significantly high value of saturation magnetization even at 20 K (Figure 6.9a). On the contrary, other fluorinating agents show antiferromagnetic nature at 20 K, while the induced magnetization appears to have a weak magnetization and butterfly-like noisy response at 300 K (Figure 6.9b). With repeated M-H measurements, it is observed that the weak moment of sample and diamagnetic moment of sample holder seems to compete with each other, giving rise to noise in the measured data, thus making separation of sample feature difficult. However, it clearly shows the contrasting behavior of F-TEDA and other fluorinating agents. Both TBABF$_4$ and NaF behave similarly and tend to be weakly ferromagnetic at 300 K (Figure 6.9b). TBABF$_4$ and NaF show perfect antiferromagnetic behavior while in other cases, an antiferromagnetic moment at 20 K is observed to be noisy. It could possibly be due to the variations in surface properties. The low coercivity (124.55 Oe) and extremely high value of saturation magnetization (4.46 Oe) of α-Fe$_2$O$_3$ with F-TEDA-20% can be accounted by the improved ferromagnetic properties at room temperature and needs further attention.
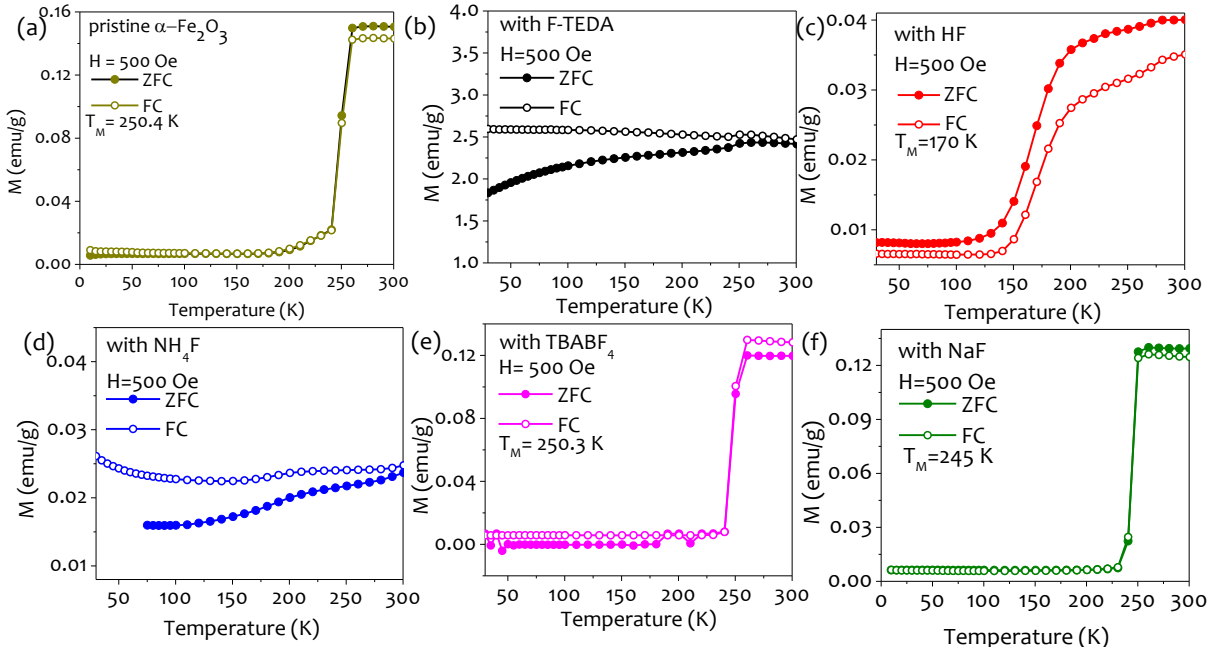
Figure 6.10: Zero-field cooled and field-cooled magnetic measurements at 500 Oe applied field for (a) pristine α-Fe_2O_3 and fluorinated Fe_2O_3 synthesized with (b) F-TEDA-20%, (c) HF-20%, (d) NH_4F-20%, (e) $TBABF_4$-20% and (f) NaF-20%.

To understand the variations in M-H curves as well as study the effect of fluorination on Morin transition temperature of α-Fe_2O_3, zero-field cooled (ZFC) and field-cooled (FC) magnetization were performed (Figure 6.10). The samples were initially cooled to 20 K in zero field and a field of 500 Oe was set at 20 K, and then the moment was taken upon heating up to 300 K and cooling down from 300 K to 20 K. Pristine α-Fe_2O_3 shows a sharp Morin transition at 250.4 K due to antiferromagnetic to weakly ferromagnetic transition, as shown in Figure 6.10a. The Morin transition temperature of pristine α-Fe_2O_3 is lower than the bulk temperature (260 K) due to dendritic nanostructure [Li et al., 2009]. At temperatures below Morin transition, α-Fe_2O_3 spins oriented along the trigonal [111] axis in the antiferromagnetic state are flipped to lie in the basal plane perpendicular to [111] axis; however, the spins are canted out of the plane, giving rise to a weak ferromagnetic moment. The ZFC and FC curve appears to be drastically different for F-TEDA and HF based Fe_2O_3. In case of F-TEDA (Figure 6.10b), the ZFC and FC magnetization curves split into two significant curves. The Morin transition at a relatively lower temperature of ~245 K in case of F-TEDA with respect to pristine is probably due to the reduction in inter-particle interaction with the introduction of surface fluorine [Liu et al., 2012]. However, the net magnetic moment is high even at low temperatures clearly indicating the alignment of spins even in frozen state. On the contrary, HF (Figure 6.10c) clearly shows a Morin transition similar to pristine but at a low temperature of 170 K with very low values of magnetization, which is also observed in M-H plot. This is due to the reduction in size of dendrites due to etching without any fluorination. The shape of ZFC and FC curves for NH_4F (Figure 6.10d) somewhat resembles F-TEDA; however, the value of magnetization is two orders lower in magnitude due to the absence of surface fluorine. For NH_4F, this weakly ferromagnetic behavior, even at low temperature could be due to the changes in morphology as seen by the presence of globular structures along with dendrites. $TBABF_4$ (Figure 6.10e) and NaF (Figure 6.10f) behave similar to pristine α-Fe_2O_3 as expected since there is no morphological or structural effects observed in these cases.
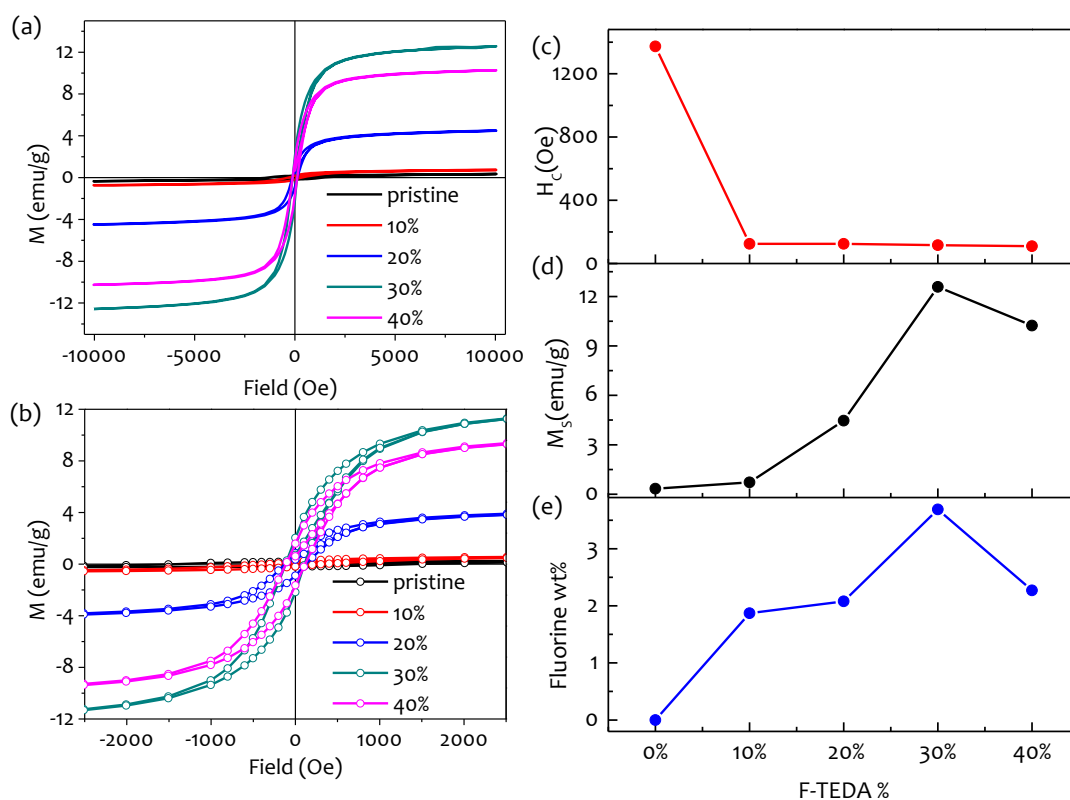
Figure 6.11 (a) Room-temperature magnetization M–H curves of the α-Fe$_2$O$_3$ with different percentage of F-TEDA: 0%, 10%, 20%, 30%, and 40% (b) Magnified view of low-field region of M-H curves at 300 K and (c) H$_C$ and (d) M$_S$ along with (e) Fluorine wt% for different percentage of F-TEDA.

For further understanding the magnetic property arising from F-TEDA, α-Fe$_2$O$_3$ with different amounts of fluorine content (i.e., F-TEDA-10%, F-TEDA-20%, F-TEDA-30%, and F-TEDA-40%) were studied (Figure 6.11a). The magnified M-H curves (in the range of $\pm$2500 Oe) show an increase in magnetization at higher applied magnetic fields with increasing concentration of F-TEDA up to 30% beyond which it decreases (Figure 6.11b). Similarly, the coercivity decreases to 115.7 Oe with increasing F-TEDA% up to 30% and remains low without any significant change in its value for 40% F-TEDA (Figure 6.11c). However, the saturation magnetization increases up to 30% F-TEDA, exhibiting a regular increase in ferromagnetic nature. Saturation magnetization reaches its highest value of 14.04 emu/g at F-TEDA-30%, and on further increasing the F-TEDA concentration, the saturation magnetization decreases (Figure 6.11d). This is directly related to the increase in the fluorine weight% for fluorination up to 30% beyond which the fluorine content decreases (Figure 6.11e). Upon fluorination with F-TEDA, surface adsorbed hydroxyl groups on α-Fe$_2$O$_3$ are replaced by the F atoms. With an increase in fluorine content (wt%), there are more surface spins that induce moments through exchange coupling between the interface surface spins and the core spins of α-Fe$_2$O$_3$, thus enhancing the overall saturation magnetization (Figure 6.12).
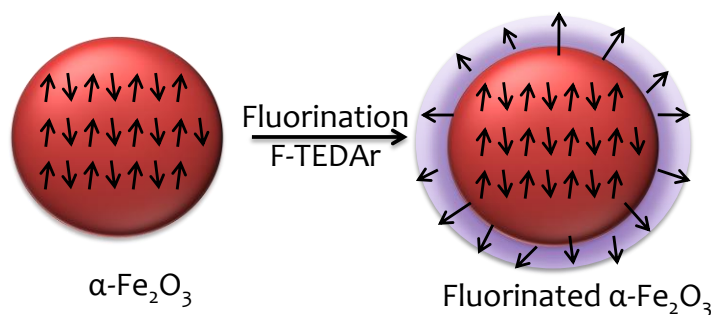

Figure 6.12: Schematic showing the pristine α-Fe$_2$O$_3$ with canted spins, which upon fluorination with F-TEDA becomes ferromagnetic due to uncompensated spins on the surface of α-Fe$_2$O$_3$ due to additional fluorine atoms. Note that spherical shape is used as a model system in place of dendritic morphology, and the effect of surface fluorine shown as a shell around α-Fe$_2$O$_3$ is considered for the sake of clarity.

The high value of M_S of fluorinated α-Fe$_2$O$_3$ (in comparison with pristine) may have contributions from both the canting of the sub-lattice spins (weak ferromagnetism) along with uncompensated surface spins. Moreover, structural defects in the form of oxygen vacancy can also result in an additional magnetic moment with an enhanced saturation magnetization as fluorine content increases successively. The low coercivity with high magnetization at a low applied field in the case of F-TEDA-30% resembles superparamagnetic behavior; however, the particles are much bigger in size and do not fall in the superparamagnetic regime. In the case of F-TEDA-40%, there is a decrease in fluorine content (2.2 wt%) due to which the net magnetic moment is lowered without affecting the coercivity value (110 Oe).
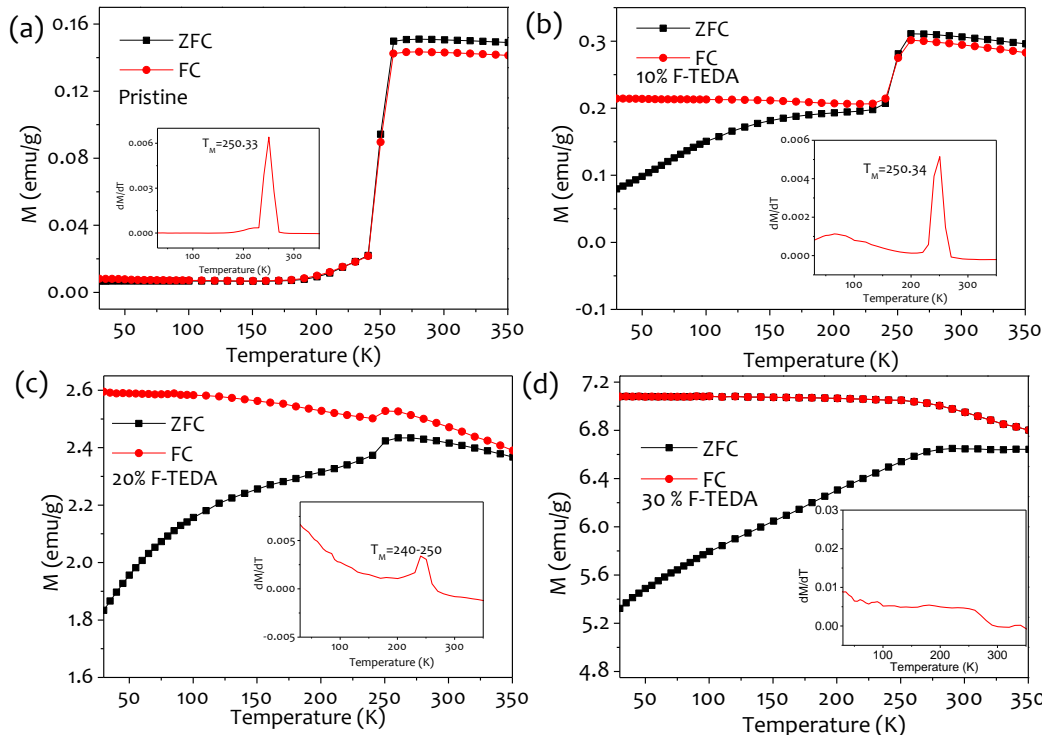

Figure 6.13: Temperature dependent magnetization at 500 Oe of α-Fe$_2$O$_3$ synthesized with different F-TEDA %; (a) 0%, (b) 10%, (c) 20% and (d) 30%. Inset shows corresponding differential ZFC curves indicating Morin Transition temperatures.

The temperature-dependent ZFC and FC magnetization curves are obtained for different percentages of F-TEDA (Figure 6.13). As observed, the splitting of ZFC and FC increases with higher F-TEDA% while the Morin transition is suppressed systematically. With increasing F-TEDA%, the Morin transition broadens over a larger temperature range and completely disappears for F-TEDA-30% (Figure 6.13a-d). The suppression in Morin transition results from possible lattice strain and defects induced by fluorination on α-Fe$_2$O$_3$ dendrites.

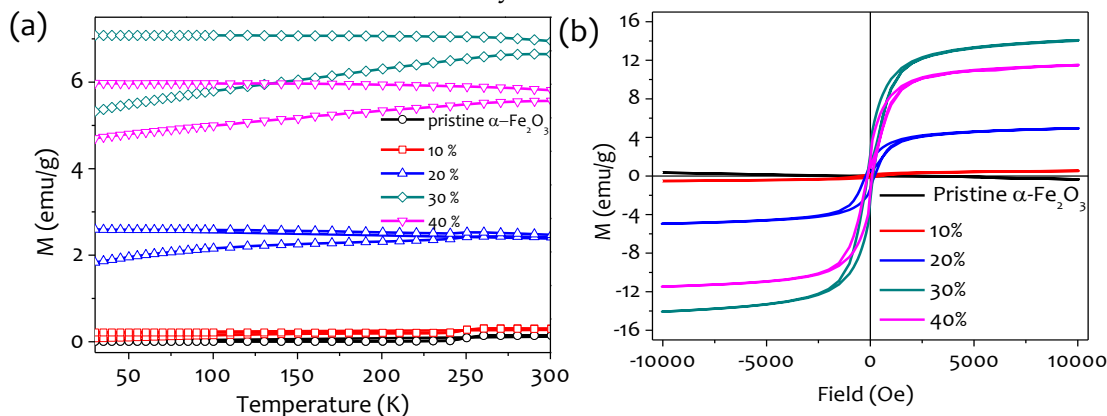**Figure 6.14:** Comparative plot of (a) temperature-dependent magnetization at 500 Oe nd (b) M–H curves of α-Fe$_2$O$_3$ synthesized with different F-TEDA percentage i.e. 0%, 10%, 20%, 30% and 40%.

The contribution of ferromagnetic interaction due to surface modification increases beyond the antiferromagnetic coupling in the core. Hence, the Morin transition strength decreases with increasing F-TEDA% (Figure 6.14a). In literature, ZFC and FC curve splitting is found to occur under superparamagnetic limit from the blocking of the moments of the individual particles; however, it is not to be confused with this case since α-Fe$_2$O$_3$ remains ferromagnetic without any significant decrease in crystallite size [Zysler et al., 2001]. The high saturation magnetization at temperatures lower than Morin transition is observed due to ferromagnetic nature of the material even at a low temperature of 20 K. (Figure 6.14b) Thus, the observed enhancement in magnetization with low coercivity for fluorinated α-Fe$_2$O$_3$ could be attributed to the uncompensated spins of surface fluorine atoms alone resulting in an increase in ferromagnetic contribution.

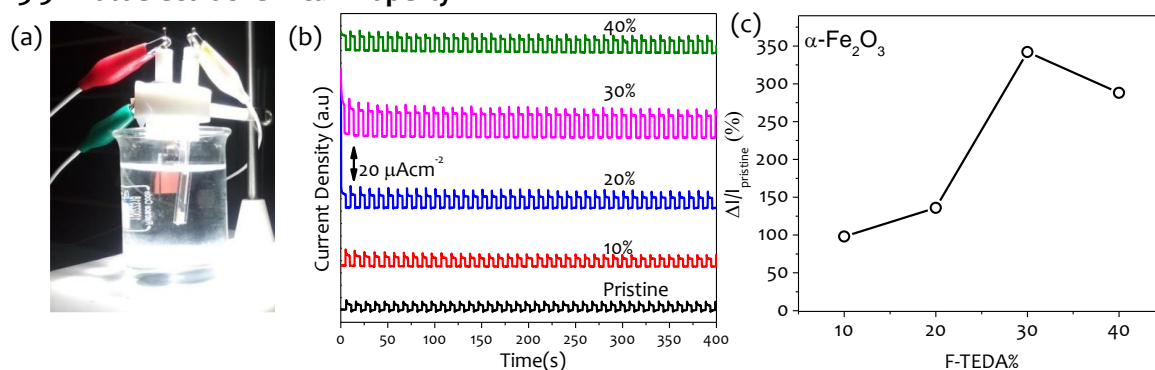**6.3.5 Photoelectrochemical Property**

Figure 6.15: Experimental setup for photoelectrochemical measurements. (b) Chronoamperometric measurements performed at 1.6 V versus RHE. (c) The photocurrent response with respect to pristine Fe$_2$O$_3$ film.

The photoelectrochemical measurements of the α-Fe$_2$O$_3$ films were performed in 1.0 M aqueous KOH solution (pH = 13.6) under 100 W/m^2 light illumination, as shown in Figure 6.15a. α-Fe$_2$O$_3$ films were prepared by screen printing a layer of an optimized thickness of ~10 μm and annealing temperature of ~500 ° C for maximum photoresponse. The pristine α-Fe$_2$O$_3$ exhibits a photocurrent density of 0.14 μA cm^{-2} at 1.23 V versus RHE. The current density for pristine α-Fe$_2$O$_3$ is very low due to the high bulk resistance as well as interfacial resistance of dendritic α-Fe$_2$O$_3$ nanostructures resulting in charge carrier accumulation at the surface leading to recombination losses. However, it is interesting to study the relative changes in the current density upon fluorination. The light on-off current taken at 1.6 V versus Ag/AgCl clearly shows a systematic increase in photocurrent over the entire voltage range upon fluorination up to 30% of F-TEDA beyond which it decreases (Figure 6.15b). This can be related to the lower at% of F atoms, as seen from the EDS analysis. Otherwise, fluorinated Fe$_2$O$_3$ with preferred (110) orientation is expected to show a higher photoelectrochemical activity with respect to pristine α-Fe$_2$O$_3$. The increase in photocurrent at higher at% of F (Figure 6.15c) may be attributed to the fact that F atoms generate charge imbalances at Fe$_2$O$_3$ surface, resulting in slower recombination of the electron-hole pairs. The electron and holes are thus available at the surface and have the better opportunity to react with water.

6.4 Conclusions

The fluorinated α-Fe$_2$O$_3$ nanostructures with dendritic morphology have been synthesized by in-situ hydrothermal method using F-TEDA as a source for electrophilic fluorine and compared with other fluoride anions precursors such as HF, NH$_4$F, TBABF$_4$ and NaF. F-TEDA is found to strongly affect the growth of α-Fe$_2$O$_3$ nanostructures resulting in snowflake-type structure with preferred (110) orientation contrary to HF that exhibits a decrease in the overall size of the dendritic nanostructures due to etching. F-TEDA exhibits a systematic increase in fluorine content, whereas no fluorine is detected in case of HF, NH$_4$F, NaF and TBABF$_4$. Interestingly,

the magnetic properties of dendritic-shaped α-Fe$_2$O$_3$ nanostructures observed in this study are contrary to observed magnetic behavior for α-Fe$_2$O$_3$ with similar morphology synthesized via same approach in literature. Upon fluorination with F-TEDA, the coercivity decreases and saturation magnetization increases systematically with increasing fluorine wt% due to transition from antiferromagnetic to ferromagnetic nature. This is attributed to the increased uncompensated surface spins of fluorine atoms. The effect of fluorination is also investigated as a photoanode in a photoelectrochemical cell. More than 300% increase in the photocurrent density was observed for 30% F-TEDA fluorinated α-Fe$_2$O$_3$ at 1.6 V versus RHE. The fluorinated α-Fe$_2$O$_3$ nanostructures developed in this study can be casted in thin films or self-assembled on substrates with the magnetic forces for various applications. These may show an appropriate magnetic resonance and exchange bias, which will be suitable for magnetic data storage and magnetic memory applications.